Photogenerated Defects in Shape-Controlled TiO$_2$ Anatase Nanocrystals: A Probe To Evaluate the Role of Crystal Facets in Photocatalytic Processes

Massimiliano D'Arienzo,*,[†] Jaime Carbajo,[‡] Ana Bahamonde,[‡] Maurizio Crippa,[†] Stefano Polizzi,[§] Roberto Scotti,[†] Laura Wahba,[†] and Franca Morazzoni[†]
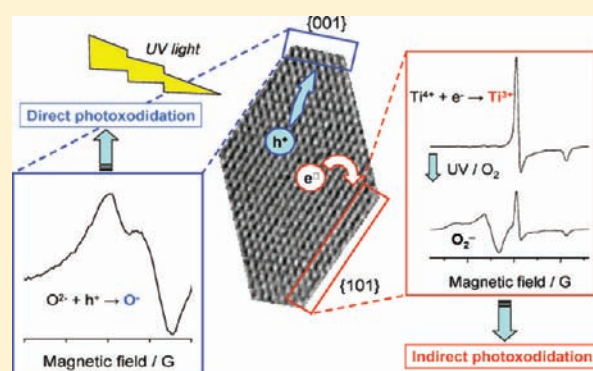
[†]INSTM, Department of Materials Science, University of Milano-Bicocca, Via R. Cozzi 53, I-20125 Milano, Italy

[‡]Instituto de Catálisis y Petroleoquímica, ICP-CSIC, C/Marie Curie No. 2, 28049 Madrid, Spain

[§]Dipartimento di Scienze Molecolari e Nanosistemi, University Ca' Foscari of Venezia, Via Torino 155/b, I-30172 Venezia-Mestre, Italy

Ⓢ *Supporting Information*

ABSTRACT: The promising properties of anatase TiO$_2$ nanocrystals exposing specific surfaces have been investigated in depth both theoretically and experimentally. However, a clear assessment of the role of the crystal faces in photocatalytic processes is still under debate. In order to clarify this issue, we have comprehensively explored the properties of the photogenerated defects and in particular their dependence on the exposed crystal faces in shape-controlled anatase. Nanocrystals were synthesized by solvothermal reaction of titanium butoxide in the presence of oleic acid and oleylamine as morphology-directing agents, and their photocatalytic performances were evaluated in the phenol mineralization in aqueous media, using O$_2$ as the oxidizing agent. The charge-trapping centers, Ti^{3+}, O$^-$, and O$_2^-$, formed by UV irradiation of the catalyst were

detected by electron spin resonance, and their abundance and reactivity were related to the exposed crystal faces and to the photoefficiency of the nanocrystals. In vacuum conditions, the concentration of trapped holes (O$^-$ centers) increases with increasing {001} surface area and photoactivity, while the amount of Ti^{3+} centers increases with the specific surface area of {101} facets, and the highest value occurs for the sample with the worst photooxidative efficacy. These results suggest that {001} surfaces can be considered essentially as oxidation sites with a key role in the photoxidation, while {101} surfaces provide reductive sites which do not directly assist the oxidative processes. Photoexcitation experiments in O$_2$ atmosphere led to the formation of Ti^{4+}–O$_2^-$ oxidant species mainly located on {101} faces, confirming the indirect contribution of these surfaces to the photooxidative processes. Although this work focuses on the properties of TiO$_2$, we expect that the presented quantitative investigation may provide a new methodological tool for a more effective evaluation of the role of metal oxide crystal faces in photocatalytic processes.

■ INTRODUCTION

Nanocrystalline TiO$_2$ is an attractive material due to its potential applications as photocatalyst in environmental pollution control, conversion and energy storage, sensors, Li batteries, photovoltaics, and so on.[1−6] The activity of titania-based photocatalysts is attributed to photogenerated electrons (e$^-$) and holes (h$^+$), located at the crystal surface, where they act as redox sources leading to the mineralization of the chemisorbed species.[2−5] Since catalyst irradiation frequently leads to proximal defects on the same particle, undesired electron−hole recombination occurs easily and suppresses the photocatalytic activity.[7−9]

Spherical TiO$_2$ nanoparticles are commonly employed as photocatalysts, due to their high surface-to-volume ratio, which guarantees a great number of surface active sites. Unfortunately, this benefit is partially quenched by the electron−hole recombination

process, favored by the small size of the crystals and by the absence of geometric anisotropy.[8,9]

By contrast, it has been demonstrated that anisotropic shaped particles, such as nanorods,[10,11] nanobelts,[12] and nanotubes,[13] would guarantee high surface area as well as a lower charge recombination rate compared to the nanospheres. This assumption arises from the hypothesis that e$^-$ and h$^+$ could in principle locate in distal parts of anisotropic nanostructures, e.g., on different crystal faces, ensuring a highly efficient charge separation.[12,13]

The photocatalytic activity not only depends on the particle shape but also is strictly related to the external surfaces exposed and, particularly, to the arrangement and coordination of the surface atoms on the different crystal facets.[14−24] Ohno et al.

reported that rutile {011} and anatase {001} faces provide the sites for oxidation, while the rutile {110} and anatase {101} faces offer the sites for reduction.[25−30] This behavior was ascribed to the presence of different energy levels of the conduction and valence bands associated with the different faces because of the atomic arrangements characteristic of their surfaces.[25−27,29] The difference in the energy levels drives the e⁻ and h⁺ to different crystal faces, aiming to reach the most stable energy configuration and leading to a charge separation.

Recently, both computational evidence[17,18,30−32] and experimental results[20,33,34] suggested that the enhanced reactivity of the anatase {001} face for the dissociative adsorption of water is related both to the high density of surface-undercoordinated Ti centers and to the presence of enlarged Ti—O—Ti bond angles at the surface, which makes titanium and oxygen centers very reactive.[18]

These results have stimulated significant research efforts toward the synthesis of anatase nanocrystals with a relevant area of exposed {001} faces.[17,20,35−40] For instance, Lu et al. successfully obtained anatase crystals with 47% {001} faces, and these showed high photoefficiency.[17] Li et al. synthesized anatase nanoparticles with dominant {001} faces, which displayed photocatalytic activity higher than that of nanoparticles with predominant {101} faces, in the oxidation of toluene and benzaldehyde.[37,38]

In contrast with the previous results, other investigations recently revealed that anatase nanocrystals with well-faceted {101} surfaces exhibit enhanced photocatalytic activity.[12,29,41] For instance, Wu et al. synthesized anatase nanoparticles with dominant {101} crystal faces, having high photoactivity and a lower electron—hole recombination rate than anatase nanospheres with an identical crystal phase and a similar specific surface area.[12] Accordingly, Murakami et al. observed high photocatalytic activity in the decomposition of acetaldehyde on anatase nanocrystals with a large {101} surface area and a small {001} area.[29]

In this scenario, it seems to us that some contradictory interpretations concerning the catalytic activity mediated by shape-controlled particles arise from insufficient characterization work addressing how the crystalline facets exposed by TiO₂ nanocrystals affect the stability and the reactivity of the paramagnetic species formed upon UV excitation. In fact, though the mentioned studies agree that the photoactivity of TiO₂ nanocrystals can be tailored by fine-tuning the particle morphology and, specifically, the exposed specific crystal faces, and though clever reports attribute to undercoordinated Ti centers and to distorted O—Ti—O moieties the responsibility for the enhanced reactivity, there is hardly any investigation which directly relates the reactivity of the different faces with the type, the amount, and the location of the electronic defects, e⁻ and h⁺, which are active promoters in photocatalysis.

In an attempt to answer the above queries, the present study associates the surface properties of anatase shape-controlled nanocrystals, having specific exposed crystal faces, to the photogenerated defects and to their photocatalytic activity. Spherical particles, nanobars, and rhombic and rhombic elongated nanocrystals were obtained by solvothermal reaction of titanium butoxide precursor (TB) in the presence of oleic acid (OA) and oleylamine (OM).[42] The OA and OM selective binding to different crystal faces drives the growth of the nanocrystals along specific crystallographic directions, depending on the TB/OA/OM ratio and the reaction temperature.

After complete removal of the excess of capping agents bound to the surfaces, the photocatalytic performances of the differently shaped titania samples were measured in the phenol mineralization, using O₂ as the oxidizing agent, and then related with the prominent faces of the nanocrystals.

The charge-trapping centers, Ti³⁺, O⁻, and O₂⁻, formed by UV irradiation of the catalyst were detected by electron spin resonance (ESR), and their abundance was related to the exposed crystal faces and in turn to the photoefficiency of the nanocrystals. To the best of our knowledge, this is the first time that the properties of the photogenerated defects have been used as a probe to evaluate the contribution of the morphology, and specifically of the crystal faces, to the photocatalytic processes.

■ EXPERIMENTAL SECTION

Chemicals. Titanium(IV) butoxide (Ti(OBu)₄ or TB, 97%), oleic acid (C₁₈H₃₃CO₂H or OA, 90%), oleylamine (C₁₈H₃₅NH₂ or OM, 70%), and superhydride solution (1 M lithium triethylboronhydride, LiEt₃BH, in THF) were all purchased from Aldrich and used without further purification.

Synthesis of Shape-Controlled TiO₂ Nanocrystals. Solvothermal synthesis of shape-controlled anatase nanocrystals was performed according to a previously reported procedure,[42] reacting TB in the presence of OA and OM. The synthesis method is based on the selective binding of OA to the anatase {001} face and of OM to the anatase {101} face, which restricts the growth to the corresponding direction. However, OA and OM act not only as capping agents but also as an acid—base pair catalyst, increasing the condensation rate without affecting the hydrolysis rate. Moreover, OA can react with TB or hydroxyalkoxide to generate carboxyalkoxide species which slow down the hydrolytic condensation process. OM, conversely, can promote the non-hydrolytic condensation process by aminolysis reaction with titanium carboxylalkoxide. Exploiting all the above properties, by simply changing the TB/OA/OM molar ratio and the reaction temperature, anatase nanocrystals with well-defined morphology were obtained.[42]

In a typical experiment, TB (22 or 44 mmol) was added to a mixture of X mmol of OA, Y mmol of OM (where X + Y = 217.5), in 25 mL of absolute ethanol. X and Y were varied to gain different TB/OA/OM molar ratios, which led to differently shaped nanocrystals: rhombic (R, TB/OA/OM = 1:4:6), rhombic elongated (RE, TB/OA/OM = 2:4:6), spherical (SP, TB/OA/OM = 1:6:4), and small nanobars (NB, TB/OA/OM = 1:8:2). For example, to synthesize TiO₂ with rhombic shape, 22 mmol of TB was added to a mixture of 88 mmol of OA, 132 mmol of OM, and 25 mL of absolute ethanol. The obtained mixture was stirred for 15 min and then transferred into a 400 mL Teflon-lined stainless steel autoclave containing 85 mL of absolute ethanol and 3.5 mL of Milli-Q water. The system was then heated to 140 or 180 °C for 18 h. After decantation, TiO₂ powder was recovered from the autoclave, washed several times with ethanol, filtered, and finally dried under vacuum (p < 10⁻² mbar) at room temperature. Hereafter, TiO₂ nanoparticles with rhombic, rhombic elongated, spherical, and nanobar shapes are labeled as R, RE, S, and NB, respectively.

Removal of Capping Agent Residuals from the TiO₂ Nanocrystals. In order to avoid catalyst deactivation due to the presence of remnants OA and OM strongly bonded to the titania surface, the following steps were performed.

First, dried TiO₂ nanocrystals were placed in a 100-mL round-bottomed flask under an argon atmosphere. Next, 10 mL of superhydride solution was added dropwise under vigorous stirring at room temperature; hydrogen gas release was observed due to reduction of the OA on the surface of the TiO₂ nanocrystals.[43] After complete addition of the superhydride solution, the resulting blue suspension underwent an ultrasound treatment for 30 min and was kept overnight under stirring at room temperature. In order to remove the unreacted superhydride and the residual traces of THF, each sample was washed with Milli-Q water

(two times with 10 mL), acetone (10 mL), and CH_2Cl_2 (two times with 10 mL).

To eliminate the excess of OM still coordinated to the surface, dried nanocrystals were then resuspended in 250 mL of 0.4 M H_2SO_4 solution and treated under ultrasound for 30 min. The resulting naked TiO_2 nanocrystals were collected by centrifugation, washed two times with 10 mL of CH_2Cl_2, and dried under vacuum ($p < 10^{-2}$ mbar) at room temperature.

Material Characterizations. Transmission electron microscopy (TEM) and high-resolution TEM (HRTEM) images and selected area electron diffraction (SAED) patterns were obtained by using a Jeol 3010 apparatus operating at 300 kV with a high-resolution pole piece (0.17 nm point-to-point resolution) and equipped with a Gatan slow-scan 794 CCD camera. Samples were prepared by placing a 5 μL drop of a dilute toluene dispersion of the nanocrystals on a holey carbon film supported on a 3 mm copper grid.

According to the model developed by Jaroniec et al. for anatase TiO_2 nanoparticles,[44] the percentage of exposed {001} faces for R and RE nanocrystals was calculated by the following equation:

$$\%S\{001\}_{exp} = S\{001\}/(S\{101\} + S\{001\}$$
$$= 2b^2/[2b^2 + (a + b)(a - b)\tan(68.3°)]\times100 \quad (1)$$

where 68.3° is the angle between the {101} and the {001} faces, and a and b correspond to the minimum and maximums side of the square {001} faces in anatase (Supporting Information, Figure S1A). The NB shape was approximately that of a rectangular parallelepiped (Supporting Information, Figure S1B), and the percentage of exposed {001} faces was simply estimated by the following equation:

$$\%S\{001\}_{exp} = S\{001\}/(S\{101\} + S\{001\}$$
$$= 2w^2/[4lw + 2w^2] \times 100 \quad (2)$$

where w and l correspond to the sides of the {001} and of the poorly pronounced {101} faces, respectively. The average values of a, b, l, and w were evaluated by measuring the sizes of ~100 particles in TEM images.

The crystal structure of the shape-controlled TiO_2 nanocrystals was determined from the X-ray diffraction (XRD) patterns collected with a Bruker D8 Advance diffractometer (Cu Kα radiation) in the range 20–60° 2θ (2θ step 0.025°, count time of 2 s/step). The diffraction peaks were indexed as pure anatase (JCPDS, no. 21-1272), and the average crystallite size was estimated from the broadening of the [101] XRD peak of anatase by using the Scherrer equation.

In order to verify the complete removal of the residual capping agents, thermogravimetric analysis (TGA) and differential scanning calorimetry (DSC) measurements before and after the cleaning procedure were performed. TGA thermograms and DSC curves were collected by using a Mettler Toledo TGA/DSC1 STARe system at constant gas flow (50 cm^3 min^{-1}). The sample powders were heated in air from 30 to 1000 °C at a heating rate of 10 °C min^{-1}. TGA curves were used to determine the temperature-dependent mass loss of the capping agents, giving an indication of the strong interaction of these molecules with the catalytic surface.

Nitrogen physisorption measurements were carried out by using a Quantachrome Autosorb-1 apparatus. The specific surface area (SSA, BET method),[45] pore volume (desorption cumulative pore volume, DCPV), and pore size distribution (BJH method)[46] were measured after evacuation at 200 °C for 16 h.

Photocatalytic Experiments. Photodegradation experiments were carried out in a 600 mL Pyrex discontinuous batch reactor equipped with an external cooling jacket, enveloped by aluminum foil, and a 125 W Hg high-pressure UV lamp placed in a coaxial quartz cylinder. No optical filter was adopted. Titanium dioxide nanocrystals (160 ± 5 mg) were suspended by ultrasound treatment in 600 mL of
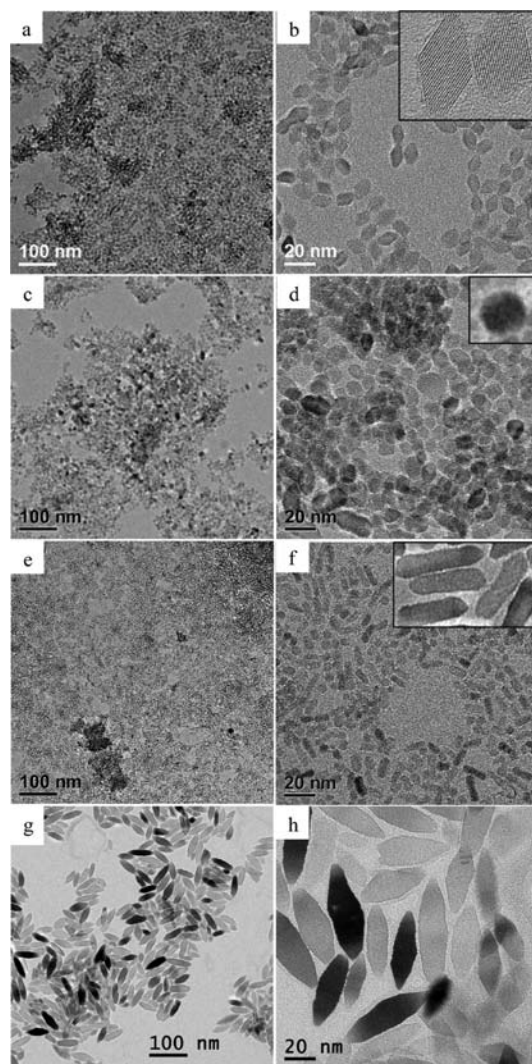

Figure 1. TEM images of the shape-controlled anatase samples: (a,b) R, (c,d) SP, (e,f) NB, and (g,h) RE. Insets in panels b, d, and f are high-magnification images of the corresponding shapes of the smallest nanocrystals.

water containing 121 ± 2 ppm of PhOH (93 ± 2 ppm as C). The temperature was kept at 25 ± 2 °C, and the suspension was recirculated by a peristaltic pump (14 mL s^{-1}). Photodegradation was performed in the presence of O_2 as oxidative agent. The slurry was saturated in an online chamber by continuously bubbling oxygen (with a constant feed of 100 mL min^{-1}) and circulated in the dark for 30 min before the UV source was turned on. The excess gas was eliminated through a non return check valve. Control experiments were carried out in the absence of TiO_2 (blank). To monitor the photoinduced degradation of phenol, aliquots (6 mL) of the reaction solution were removed at regular intervals and after centrifugation, and the clear solutions were analyzed for the total organic carbon (TOC) using a Shimadzu TOC-V CSH analyzer.

Electron Spin Resonance Spectroscopy. The ESR investigation was performed by using a Bruker EMX spectrometer operating at the X-band frequency and equipped with an Oxford cryostat working in the temperature range of 4–298 K. The nanocrystals were charged in quartz glass tubes connected both to a high-vacuum pumping system and to a controlled gas feed (O_2). Spectra were recorded under in vacuo conditions (10^{-5} mbar) at 130 K, before and after 30 min of UV irradiation inside the ESR cavity at the same temperature.
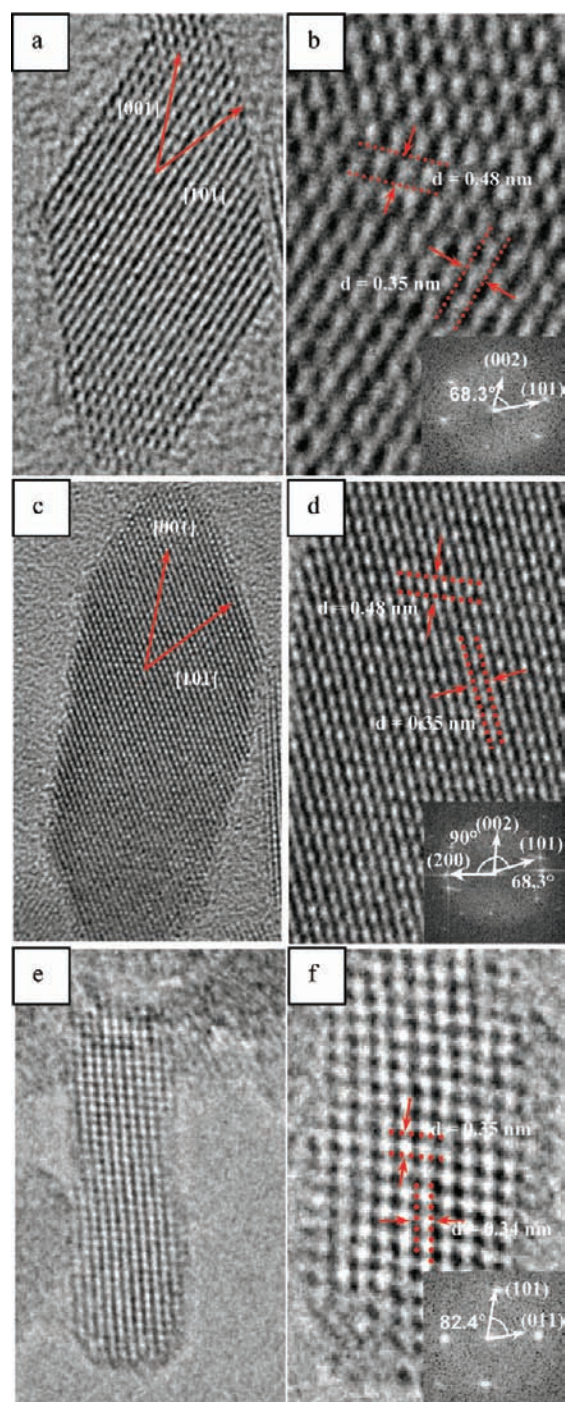
Figure 2. Representative HRTEM images of the *R* (a,b), *RE* (c,d), and *NB* (e,f) samples. The insets are the FFT images of the corresponding nanoparticles.

The experimental procedure lowers the recombination of the photogenerated species. For each sample, the absence of a signal before irradiation was checked. No significant differences resulted between the spectra recorded just before and 20 min after switching off the UV irradiation, except a small decrease of the signal intensity. Spectra were acquired with a modulation frequency of 100 kHz, modulation amplitudes of 2−5 G, and microwave powers of 2−5 mW. Irradiation was performed by using a 150 W Xe UV lamp (Oriel) with the output radiation focused on the samples in the cavity by an optical fiber (50 cm length, 0.3 cm diameter). The *g* values were calculated by standardization with α,α'-diphenyl-β-picryl hydrazyl (DPPH). The spin concentration was obtained by double integration of the resonance lines, referring to the area of the standard Bruker weak pitch ($9.7 \times 10^{12} \pm 5\%$ spins cm^{-1}). Accuracy on double integration was ±15%. Care was taken to always keep the most sensitive part of the ESR cavity (1 cm length) filled. Spectra simulations and fits were performed using the SIM 32 program.[47]

■ RESULTS AND DISCUSSION

Structural and Morphological Characterization. Figure 1 summarizes the TEM investigation performed on the anatase shape-controlled nanoparticles. According to the results reported by Dihn et al.,[42] when the reaction is carried out at 180 °C and with low OA/OM ratio (TB/OA/OM = 1:4:6), *R* TiO_2 nanoparticles that are very homogeneous in shape and size (13.5 nm length) are obtained (Figure 1a,b). At the same reaction temperature, increasing the OA/OM ratio and leaving unchanged the concentration of the titanium precursor (TB/OA/OM = 1:6:4), almost *S* nanocrystals with mean diameter of 9.5 nm are produced (Figure 1c,d). Further increasing the OA concentration (TB/OA/OM = 1:8:2) at a lower reaction temperature (140 °C) leads to the formation of small *NB* TiO_2, 13 nm long (Figure 1e,f). Finally, under the same reaction conditions used to obtain the *R* shaped nanoparticles, but with double the amount of titanium precursor (TB/OA/OM = 2:4:6), the formation of large *RE* particles is observed (Figure 1g,h), which are less uniform in size (average length 45−60 nm).

In order to study in detail the shape and the exposed crystal faces, HRTEM images of *R*, *RE*, and *NB* TiO_2 nanocrystals were collected (Figure 2). In particular, higher magnifications (Figure 2b,d) of *R* and *RE* lattice fringes along the [010] direction clearly reveal the presence of (101) and (002) crystallographic planes with lattice space of 0.35 and 0.48 nm, respectively. The angles indicated in the corresponding fast Fourier transform (FFT) images (insets in Figure 2b,d) are ∼68.3° and ∼90°, which are identical to the theoretical values for the angles between the {101} and {001} faces and between the {100} and {001} faces, respectively. This information confirms that the *R* and *RE* anatase nanocrystals mainly expose {001} and {101} surfaces, with the additional presence for *RE* nanocrystals of a small amount of exposed {100} and {010} faces.

Table 1. Structural Parameters and Catalytic Performances of Shape-Controlled TiO_2 Nanocrystals

sample	L_{XRD} (nm)	pore volume (DCPV, $cm^3\,g^{-1}$)	SSA_{BET} ($m^2\,g^{-1}$)	exposed {001} crystal facets (%)	exposed {101} crystal facets (%)	SSA_{BET} of exposed {001} crystal facets ($m^2\,g^{-1}$)	SSA_{BET} of exposed {101} crystal facets ($m^2\,g^{-1}$)	$t_{1/2}$ (min)
SP	7.6	0.47	178.8					130.0
NB	7.3	0.27	227.0	5.8	94.2	13.1	213.8	183.7
R	13.1	0.35	199.0	10.6	89.4	21.2	177.9	89.3
RE	16.5	0.21	170.5	9.2	90.8	15.7	154.8[a]	124.1

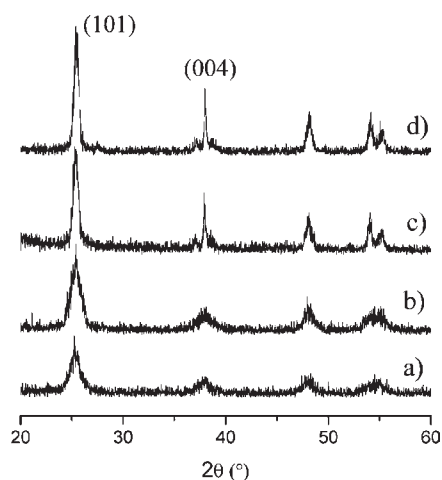[a] Included the {010} and {100} minority facets.

Figure 3. XRD patterns of (a) spherical (*SP*), (b) nanobars (*NB*), (c) rhombic elongated (*RE*), and (d) rhombic (*R*) TiO$_2$ nanocrystals collected after the removal of capping agents.
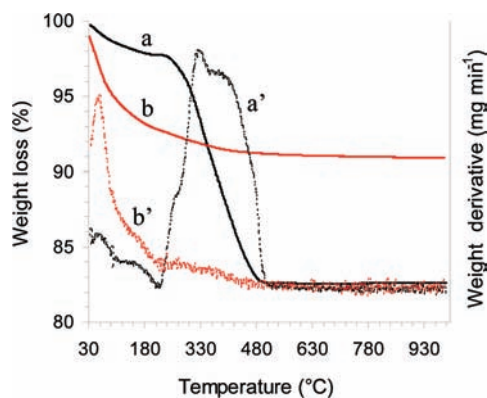

Figure 4. TGA curves and corresponding derivative thermogravimetry profiles of *RE* nanocrystals before (a,a′, black lines) and after the cleaning procedure (b,b′, red lines) which removes the capping agents.

In the HRTEM images of *NB* nanoparticles, only the (101) and (011) atomic planes, with space of ∼0.35 nm and interfacial angle of 82.4°, are detected (Figure 2e,f). This indicates that the crystal growth occurs mainly on the {001} face, which becomes less dominant. It is also very evident that the exposed {101} faces are much less prominent than in the case of *R* and *RE* nanocrystals, and the morphology resembles that of a rectangular parallelepiped.

Based on the TEM and HRTEM analysis, average *a*, *b*, *l*, and *w* values were calculated, which correspond to the minimum and the maximum sizes of the square {001} faces in *R* and *RE* nanocrystals, and to the sides of the {001} and of the poorly pronounced {101} faces of the *NB* (Supporting Information).[44] From these values and according to eqs 1 and 2, the percentages of {001} exposed crystal faces for *R*, *RE*, and *NB* nanocrystals were estimated as 10.6, 9.2, and 5.8%, respectively (see Table 1). For *R* and *NB* nanocrystals, the remaining percentage can be easily assigned to the {101} exposed crystal faces, while for *RE* nanoparticles it represents the sum of {101}, {010}, and {100} faces. According to these calculations, we can infer that *NB* particles present a higher percentage of {101} faces than *RE* and *R* nanocrystals (Table 1).

XRD patterns (Figure 3) of all the synthesized nanocrystals after the cleaning procedure indicate the exclusive presence of
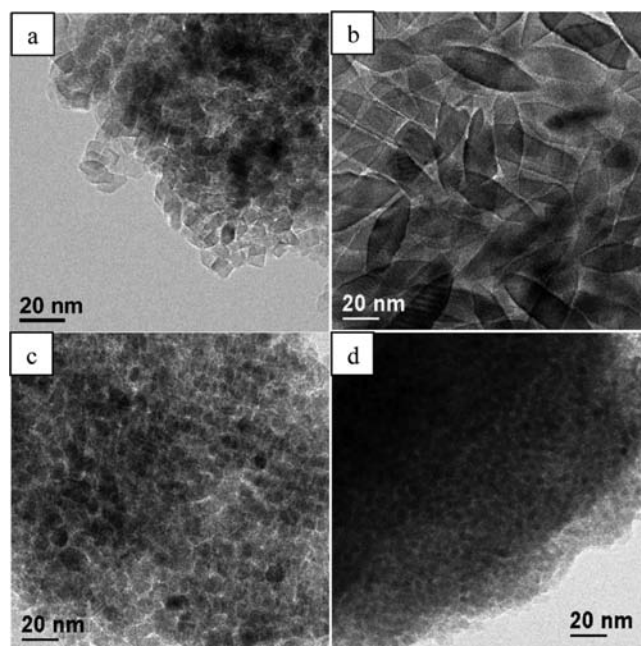

Figure 5. TEM images of (a) *R*, (b) *RE*, (c) *SP*, and (d) *NB* anatase nanocrystals after the cleaning procedure with the superhydride solution and the washing treatment with dilute sulfuric acid.
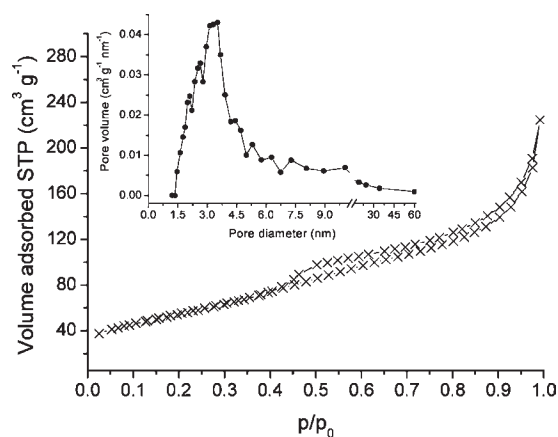

Figure 6. Adsorption−desorption isotherm at liquid nitrogen temperature for *R* TiO$_2$ nanocrystals. The curve corresponds to a type IV isotherm with capillary condensation in the mesopores. Inset: pore-size distribution.

anatase phase. A gradual increase in the relative intensity and sharpening is observed for the (004) diffraction peak on going from *SP* to *R* nanoparticles, suggesting a growth along the [001] direction. The average crystallite sizes (L_{XRD}), calculated by the Scherrer equation, agreed in general with the crystal width estimated from the TEM images (see Table 1).

TGA was performed on both as-prepared shape-controlled TiO$_2$ nanocrystals and naked particles, obtained after removal of the residual capping agents by washing with superhydride and dilute sulfuric acid solutions.[43] In particular, Figure 4 shows the weight loss curves and the corresponding derivatives of the *RE* nanocrystals before (a and a′, black lines) and after the cleaning procedure (b and b′, red lines). In the as-prepared sample (black curve a), a first small weight loss (∼2%) beginning at nearly

33 °C and continuing until 220 °C is detected and attributed to physisorbed ethanol solvent. The second largest weight loss occurs in a wide temperature range, from 230 to 510 °C, relatable to the thermal degradation of OA and OM chains. Conversely, after the cleaning procedure (red curve b), the R nanocrystals show only one small weight loss (~6%) between 33 and 220 °C, ascribed to the removal of the surface physisorbed water. These results indicate a fairly complete elimination of the organic capping agents after reduction with superhydride solution and washing with dilute sulfuric acid.

The effects of the cleaning procedure were also explored by collecting TEM images of all "naked" TiO$_2$ particles (Figure 5). Despite the increased agglomeration, the nanocrystals retain their initial morphology. The removal of the residual capping agents is a key point. In fact, the presence of organic molecules grafted to the surface of the nanocrystals hinders the contact between the target pollutants and the catalyst particles, thus preventing the application of these materials in photocatalysis. Furthermore, charge separation in organically modified TiO$_2$ nanocrystals can be greatly affected by the instantaneous transfer of holes to the organic molecules.[53] Therefore, the cleaning procedure performed here is a suitable met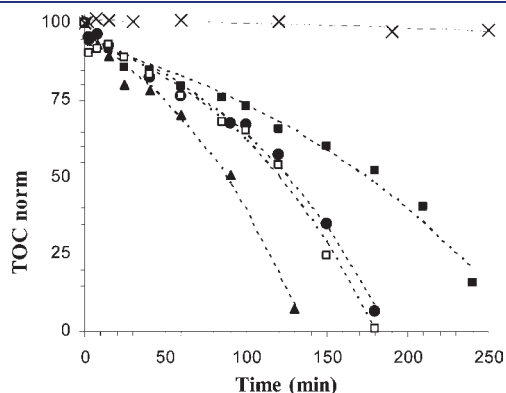hod to obtain naked nanocrystals with unchanged morphology and to avoid detrimental interferences in the charge separation and photocatalytic properties.

Nitrogen physisorption experiments were performed on all the shape-controlled TiO$_2$ nanocrystals after the removal of the capping agents. All samples are mesoporous and show a type IV Brunauer isotherm. As an example, the adsorption–desorption isotherms and the corresponding monomodal pore-size distribution of R-shaped nanoparticles are shown in Figure 6. According to the t-plot, no micropores were detected.

The specific surface areas (SSA$_{BET}$) and BJH pore volumes (DCPV) of differently shaped TiO$_2$ nanocrystals are reported in Table 1. Using the percentage of the mainly exposed {001} and {101} crystal faces, their relative SSA$_{BET}$ were also calculated.

Photocatalytic Activity. The photocatalytic activity of the shape-controlled TiO$_2$ nanocrystals was evaluated in the phenol mineralization employing O$_2$ as oxidizing agent under UV irradiation (see Experimental Section). In all the performed experiments, during the initial stage of recirculation in the dark (30 min), phenol adsorption on the nanoparticle surfaces causes depletion of the loaded PhOH by about 5.0 ± 2%. The data of TOC disappearance and the fitted curves[55] of PhOH mineralization for shape-controlled TiO$_2$ nanocrystals are shown in Figure 7. The *Blank* test is also reported for comparison. In order to compare the mineralization kinetics of the different samples, the half degradation time value $t_{1/2}$, normalized on the same mass of catalyst (160 mg), was taken as a representative parameter (Table 1). The experimental uncertainty of $t_{1/2}$ does not exceed ±7 min.

The photocatalytic activity of the anatase nanocrystals was greatly dependent on the particle shape (Figure 7). In particular, the best performance occurs for the sample consisting of very uniform R-shaped particles, which also display a relatively high SSA and the largest pore volume. Despite having the lowest SSA$_{BET}$ and DCPV (see Table 1), large RE nanocrystals show relevant activity too, higher than SP and NB samples. Finally, despite the very high SSA (227 m^2 g^{-1}) and a moderately high pore volume, small NBs exhibit the worst photoefficiency. These results suggest that the differences in the particle size, total surface area, and porosity among TiO$_2$ nanocrystals are not representative of their photocatalytic properties, while the

Figure 7. Mineralization curves of phenol (given as TOC%) under UV irradiation in the presence of O$_2$ of (×) *Blank*, without catalyst, (■) *NB*, (●) *SP*, (□) *RE*, and (▲) *R* TiO$_2$ nanocrystals.
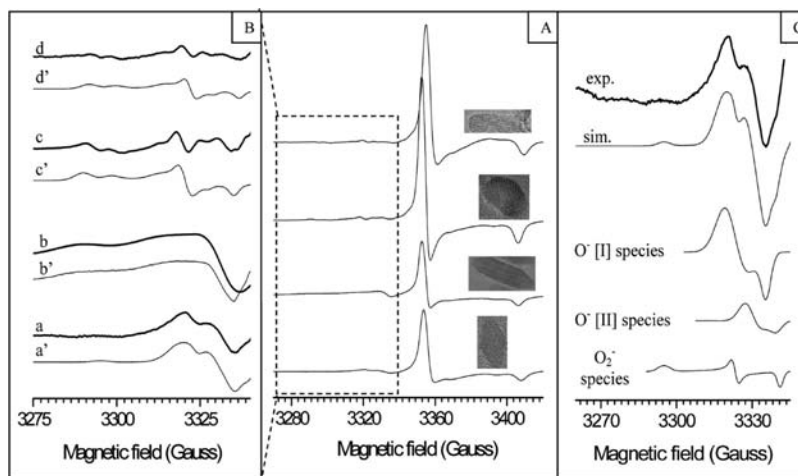

Figure 8. (A) Experimental ESR spectra of differently shaped TiO$_2$ nanocrystals. Insets show the corresponding shapes. (B) Magnification of the O$^-$ spectral region: experimental (a–d) and simulated (a′–d′) ESR spectra. (C) Deconvolution (sim.) of ESR signals of *R* nanoparticles (exp.) into O$^-$ and O$_2^-$ species.

Table 2. g Tensor Values of the Paramagnetic Defects Detected after Photoexcitation in a Vacuum ($p < 10^{-5}$ mbar) in Shape-Controlled TiO$_2$ Nanocrystals, Determined by Simulation of the ESR Features, along with the Relative Contribution of the O$^-$ Species (Calculated as % of the Total Intensity of the O$^-$ + O$_2^-$ Signals)

| sample	O$^-$ centers	O$^-$ species	Ti^{3+} species	O$_2^-$ species
NB	2%	$g_\perp = 2.0126$, $g_\parallel = 2.0046$	$g_\perp = 1.9867$ $g_\parallel = 1.9570$	O$_2^-$[I]: $g_{zz} = 2.0252$, $g_{yy} = 2.0080$, $g_{xx} = 1.9990$ O$_2^-$[II]: $g_{zz} = 2.0212$, $g_{yy} = 2.0080$, $g_{xx} = 1.9990$
SP	1%	$g_\perp = 2.0129$, $g_\parallel = 2.0047$	$g_\perp = 1.9876$ $g_\parallel = 1.9579$	O$_2^-$[I]: $g_{zz} = 2.0254$, $g_{yy} = 2.0083$, $g_{xx} = 1.9990$ O$_2^-$[II]: $g_{zz} = 2.0215$, $g_{yy} = 2.0083$, $g_{xx} = 1.9990$
R	78%	O$^-$[I]: $g_\perp = 2.0090$, $g_\parallel = 2.0001$ O$^-$[II]: $g_\perp = 2.0050$, $g_\parallel = 1.9975$	$g_\perp = 1.9866$ $g_\parallel = 1.9575$	$g_{zz} = 2.0258$, $g_{yy} = 2.0072$, $g_{xx} = 1.9965$
RE	44%	$g_\perp = 2.0090$, $g_\parallel = 2.0004$	$g_\perp = 1.9866$ $g_\parallel = 1.9582$	$g_{zz} = 2.0280$, $g_{yy} = 2.0070$, $g_{xx} = 1.9994$
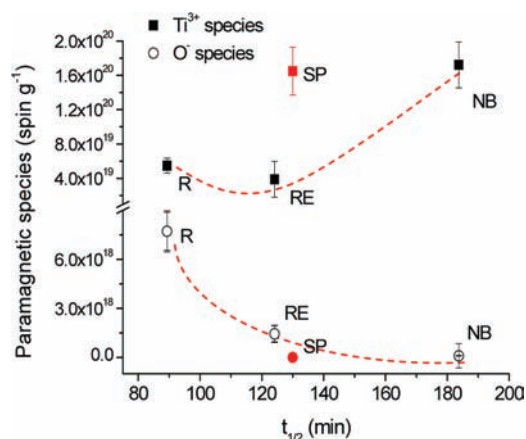
Figure 9. Trends of the relative amounts of O$^-$ species (○) and Ti^{3+} species (■) calculated for differently shaped TiO$_2$ nanocrystals vs half transformation times ($t_{1/2}$).

morphology (see Morphological Characterization), the exposed crystal faces, and their relative SSA seem to play the major roles.

In detail, the large SSA$_{BET}$ of the exposed {001} faces and the relatively high area of the exposed {101} faces (Table 1) appear crucial in determining the remarkable photocatalytic activity of R and RE nanocrystals. This is in agreement with previous studies indicating {001} faces as oxidation sites and describing improved photoxidation properties in the presence of large amounts of these surfaces.[17,20,35−40]

Conversely, the low SSA of exposed {001} crystal faces and the remarkably high area of {101} surfaces, attributed to the small dimension of NB nanocrystals, provide fewer oxidation sites and easy electron−hole recombination.[8,9] SP nanoparticles (mean diameter = 9.5 nm) display an intermediate catalytic efficiency, much higher than that of NB while lower than those of R and RE. This cannot be related to either enhanced porosity or the exposition of different crystals faces (difficult to discriminate by TEM or HRTEM), while the electronic properties of these nanoparticles can account for this behavior (see ESR Investigation).

ESR Investigation. In order to study how the exposition of specific crystal faces affects the stability and the reactivity of the charge-trapping centers formed upon UV excitation and, in turn, the photoactivity of R, RE, S, and NB nanocrystals, ESR spectra
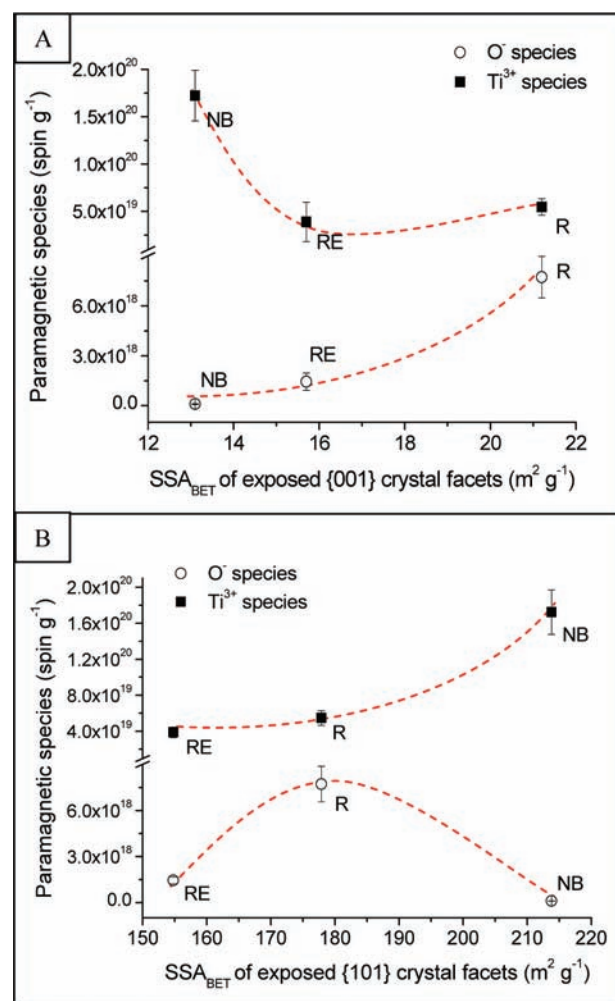
Figure 10. Trends of the relative abundance of O$^-$ and Ti^{3+} species for R, RE, and NB TiO$_2$ nanocrystals as a function of the specific surface area (SSA$_{BET}$) of their {001} (A) and {101} (B) exposed crystal faces.

were acquired after UV irradiation at 130 K, either in vacuo ($p < 10^{-5}$ mbar) or in the presence of $p(O_2) = 10$ mbar.

After irradiation under vacuum (Figure 8), all samples show two well-separated sets of resonance lines. The higher field sharp

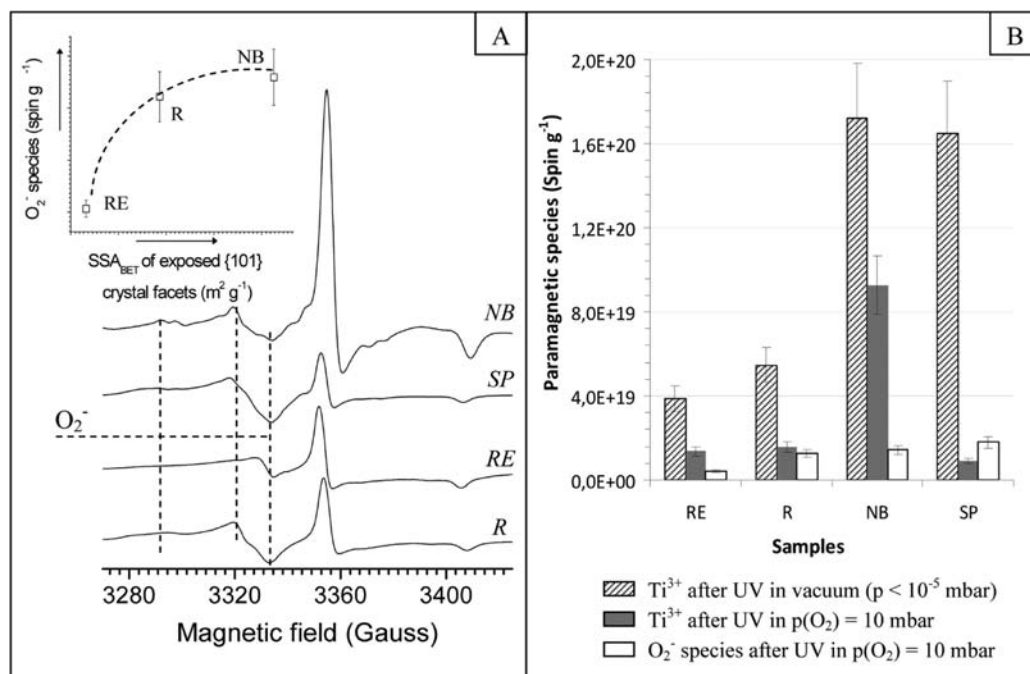**Figure 11.** (A) ESR spectra of shape-controlled anatase nanoparticles at 130 K after UV irradiation in the presence of 10 mbar of O_2 and then under a vacuum at $p < 10^{-5}$ mbar. The inset shows the trend of the abundance of superoxide species (O_2^-) as a function of the SSA of exposed {101} crystal faces. (B) Amount of Ti^{3+} and O_2^- species detected after UV irradiation either in a vacuum $(p < 10^{-5}$ mbar) or in the presence of $p(O_2) = 10$ mbar for differently shaped nanocrystals.

signals (Figure 8A), having axial symmetry, are characteristic of d^1 centers (Table 2) and can be assigned to electrons trapped at Ti^{3+} centers.[49−55] Their intensity is much greater than that of the lower field resonances (Figure 8B), and their sharpness suggests a crystalline environment of Ti^{3+} centers.[54] The values of the g tensor components of Ti^{3+} centers for *NB*, *RE*, and *R* nanocrystals are very similar. The g values associated with *SP* particles are instead significantly different. This suggests that the high curvature of the *SP* structure promotes a crystal field distortion of Ti^{3+} centers[56] and increases the spin−orbit coupling contribution to the g tensor components.[57]

The lower field features (Figure 8B) can be attributed to different superimposed oxygen species, O^- and O_2^-,[58,59] whose g values and relative contributions were calculated by signal simulation (Table 2). The g tensor values are slightly different, depending on the morphology of the nanocrystals. In particular, the lower field resonances occurring in *R* nanocrystals were resolved by simulating three different components (Figure 8C): one orthorhombic line attributable to a superoxide species (O_2^-) and two overlapping axial signals attributable to holes trapped at two different O^- sites $(O^-[I]$ and $O^-[II]$, see Table 2).

The presence of O_2^- species, mainly occurring in *NB* and *SP* nanocrystals, even when UV irradiation was performed under a vacuum, may be related to the evolution of residuals OH^- groups according to the following mechanism:[60]

$$h^+ + OH^- \rightarrow {}^{\bullet}OH \tag{3}$$

$$2{}^{\bullet}OH \rightarrow H_2O_2 \tag{4}$$

$$H_2O_2 + h^+ \rightarrow O_2^- + 2H^+ \tag{5}$$

$$O_2^- + h^+ \rightarrow O_2 \tag{6}$$

Considering their determinant role in oxidative catalysis (see below), the relative contribution of the O^- species (calculated as % of the total intensity of the $O^- + O_2^-$ signals) was determined and reported in Table 2 for the differently shaped nanocrystals.

The abundance and stability of the paramagnetic centers detected by ESR after UV irradiation can be related to the charge separation and to their inhibited recombination.[49−55] Hence, as already described in our previous studies,[54,55] the amount of charge carriers allows us to determine the overall quantum efficiency of the catalytic process. In order to associate the paramagnetic defects with the photocatalytic efficacy, it has to be stressed that, although the photocatalytic characterization had been carried out in a water solution, the ESR measurements were performed on powders. Thus ESR provides unique information on the charge separation prior to interaction with the solvent molecules.

In the present case, from the area of integrated signals obtained after photoexcitation in a vacuum, the concentration of electrons trapped on Ti^{3+} always exceeds that of holes trapped on O^-. In particular, when plotted against $t_{1/2}$, the amount of O^- centers decreases with increasing $t_{1/2}$, i.e. with decreasing photoefficiency (Figure 9). Conversely, the quantity of the photogenerated electrons trapped on Ti^{3+} sites is about 1 order of magnitude larger than that O^- and increases as $t_{1/2}$ becomes higher.

These trends clearly suggest a parallel between the photoactivity of faceted nanocrystals and the amount of trapped holes, which ultimately drives the surface photooxidation procsses. In contrast, no simple relation between the abundance of Ti^{3+} centers and the photoactivity can be suggested at this stage.

The amounts of O^- and Ti^{3+} centers for shape-controlled nanocrystals were related to the different surface area of $\{001\}$ and $\{101\}$ exposed crystal faces. In the former case it turned out that increasing the surface area of $\{001\}$ exposed faces caused the concentration of trapped holes (O^- centers) to increase and reached the maximum value for *R* nanocrystals, which show the highest photoactivity, while the amount of Ti^{3+} centers follows almost an opposite trend (Figure 10A). This suggests that $\{001\}$ faces in anatase nanoparticles with uniform shape can really be considered as privileged oxidation sites, and their role appears fundamental in enhancing the photoxidation processes.[25−30]

In the latter case (Figure 10B), the amount of Ti^{3+} centers increases with the increase of the SSA of $\{101\}$ facets and displays the highest value for the *NB* sample, which shows the worst photooxidative efficacy. The concentration of trapped holes (O^-) exhibits a different trend, with a maximum for *R* nanocrystals. These results suggest that $\{101\}$ faces in shape-controlled anatase nanocrystals can actually provide reductive sites[25−30] which do not directly assist the oxidative processes.

In order to further elucidate the role of the different crystal faces in the photooxidative processes, ESR investigations on *R*, *RE*, *SP*, and *NB* nanocrystals were performed after UV irradiation at 130 K in the presence of $p(O_2) = 10$ mbar and subsequent removal of the residual oxygen by evacuation at $p < 10^{-5}$ mbar. The resonances of Ti^{3+} and of O_2^- centers can be easily detected (Figure 11A). After oxygen contact, the intensity of the Ti^{3+} features of *SP*, *R*, and *RE* nanocrystals becomes much lower than that detected in vacuum, while for *NB* nanocrystals the concentration of Ti^{3+} centers remains high (Figure 11B). This indicates an enhanced reactivity of these traps, mainly located at the surface in *SP*, *R*, and *RE* nanoparticles, which in principle are able to give, by electron transfer, $Ti^{4+}-O_2^-$ species that are active in the oxidative processes.[55,58,59]

Finally, it can be observed that the amount of superoxide species is very high for *SP* nanoparticles, while for faceted nanocrystals it is generally low (Figure 11B) and increases as the SSA of exposed $\{101\}$ faces increases, becoming the highest for *NB* nanoparticles (inset in Figure 11A). This, on one hand, can explain the relatively good photoefficacy of the *SP* nanocrystals and, on the other, suggests that O_2^- species locate mainly on $\{101\}$ faces, confirming an indirect involvement of these surfaces in the photooxidative processes.

CONCLUSION

In the present study, we comprehensively investigated the stability and the reactivity of the paramagnetic defects formed upon UV excitation in shape-controlled anatase nanocrystals in order to evaluate the relative contribution of their exposed crystal facets to the photoactivity.

Trapping and interfacial transfer of photogenerated charges was greatly affected by the specific exposed surfaces of the nanocrystals. In particular, after photoexcitation in vacuum, the concentration of trapped holes (O^- centers) increases with the increase of the $\{001\}$ surface area, reaching a maximum value for *R* nanocrystals, which show the highest photoactivity. Conversely, the amount of Ti^{3+} centers increases together with the specific surface area of $\{101\}$ facets, and the highest value occurs for the *NB* samples, which exhibit the worst photooxidative efficacy. These outcomes indicate that $\{001\}$ surfaces play the major role in the photocatalytic process by providing oxidation

sites, while the $\{101\}$ surfaces, as supplier of reductive sites, are only indirectly involved.

UV excitation in an O_2 atmosphere leads to a partial annihilation of the Ti^{3+} features, mainly for *SP*, *R*, and *RE* nanocrystals, and to the formation of O_2^- species mainly located on $\{101\}$ faces, proving the indirect contribution of these surfaces to the photooxidative processes.

Therefore, by quantitatively monitoring the formation and the interfacial reactivity of the charge-trapping sites in shape-controlled anatase nanocrystals, we provided a novel tool to evaluate the role of the exposed crystal faces in the photocatalytic processes.

■ ASSOCIATED CONTENT

ⓢ Supporting Information. Details on the model exploited to calculate the percentage of exposed $\{001\}$ faces for *R*, *RE*, and *NB* anatase nanocrystals. This material is available free of charge via the Internet at http://pubs.acs.org.

■ AUTHOR INFORMATION

Corresponding Author
massimiliano.darienzo1@unimib.it

■ ACKNOWLEDGMENT

■ REFERENCES

(1) Gratzel, M. *Nature* **2001**, *414*, 338–344.
(2) Diebold, U. *Surf. Sci. Rep.* **2003**, *48*, 53–229.
(3) Thompson, T. L.; Yates, J. T. *Chem. Rev.* **2006**, *106*, 4428–4453.
(4) Chen, X.; Mao, S. S. *Chem. Rev.* **2007**, *107*, 2891–2959.
(5) Fujishima, A.; Zhang, X. T.; Tryk, D. A. *Surf. Sci. Rep.* **2008**, *63*, 515–582.
(6) Hagfeldt, A.; Boschloo, G.; Sun, L. C.; Kloo, L.; Pettersson, H. *Chem. Rev.* **2010**, *110*, 6595–6663.
(7) Grela, M.; Colussi, A. J. *J. Phys. Chem.* **1996**, *100*, 18214–18221.
(8) Zhang, Z.; Wang, C. C.; Zakaria, R.; Ying, J. Y. *J. Phys. Chem. B* **1998**, *102*, 10871–10878.
(9) Kominami, H.; Muratami, S.; Kato, J.; Kera, Y.; Ohtani, B. *J. Phys. Chem. B* **2002**, *106*, 10501–10507.
(10) Cozzoli, P. D.; Kornowski, A.; Weller, H. *J. Am. Chem. Soc.* **2003**, *125*, 14539–14548.
(11) Manna, L.; Scher, E. C.; Li, L. S.; Alivisatos, A. P. *J. Am. Chem. Soc.* **2002**, *124*, 7136–7145.
(12) Wu, N.; Wang, J.; Tafen, D. N.; Wang, H.; Zheng, J. G.; Lewis, J. P.; Liu, X.; Leonard, S. S.; Manivannan, A. *J. Am. Chem. Soc.* **2010**, *132*, 6679–6685.
(13) Riss, A.; Elser, M. J.; Bernardi, J.; Diwald, O. *J. Am. Chem. Soc.* **2009**, *131*, 6198–6206 and references therein.
(14) Yin, Y.; Alivisatos, A. P. *Nature* **2005**, *437*, 664–670.
(15) Barnard, A. S.; Curtiss, L. A. *Nano Lett.* **2005**, *5*, 1261–1266.
(16) Tian, N.; Zhou, Z. Y.; Sun, S. G.; Ding, Y.; Wang, Z. L. *Science* **2007**, *316*, 732–735.
(17) Yang, H. G.; Sun, C. H.; Qiao, S. Z.; Zou, J.; Liu, G.; Smith, S. C.; Cheng, H. M.; Lu, G. Q. *Nature* **2008**, *453*, 638–641.
(18) Selloni, A. *Nat. Mater.* **2008**, *7*, 613–615.

(19) Han, X. G.; Jin, M. S.; Xie, S. F.; Kuang, Q.; Jiang, Z. Y.; Jiang, Y. Q.; Xie, Z. X.; Zheng, L. S. *Angew. Chem, Int. Ed.* **2009**, *48*, 9180–9183.

(20) Yang, H. G.; Liu, G.; Qiao, S. Z.; Sun, C. H.; Jin, Y. G.; Smith, S. C.; Zou, J.; Cheng, H. M.; Lu, G. Q. *J. Am. Chem. Soc.* **2009**, *131*, 4078–4083.

(21) Liu, M.; Piao, L.; Zhao, L.; Ju, S.; Yan, Z.; He, T.; Zhou, C.; Wang, W. *Chem. Commun.* **2010**, *46*, 1664–1666.

(22) Pan, J.; Liu, G.; Qing, M.; Cheng, H. M. *Angew. Chem., Int. Ed.* **2011**, *50*, 2133–2137.

(23) Wen, C. Z.; Jiang, H. B.; Qiao, S. Z.; Yang, H. G.; Lu, G. Q. *J. Mater. Chem.* **2011**, *21*, 7052–7061.

(24) Fang, W. Q.; Gong, X. Q.; Yang, H. G. *J. Phys. Chem. Lett.* **2011**, *2*, 725–734.

(25) Ohno, T.; Sarukawa, K.; Matsumura, M. *New J. Chem.* **2002**, *26*, 1167–1170.

(26) Bae, E.; Murakami, N.; Ohno, T. *J. Mol. Catal. A: Chem.* **2009**, *300*, 72–79.

(27) Bae, E.; Ohno, T. *Appl. Catal., B* **2009**, *91*, 634–639.

(28) Bae, E.; Murakami, N.; Nakamura, M.; Ohno, T. *Appl. Catal., A* **2010**, *380*, 48–54.

(29) Murakami, N.; Kurihara, Y.; Tsubota, T.; Ohno, T. *J. Phys. Chem. C* **2009**, *113*, 3062–3069.

(30) Murakami, N.; Katayama, S.; Nakamura, M.; Tsubota, T.; Ohno, T. *J. Phys. Chem. C* **2011**, *115*, 419–424.

(31) Vittadini, A.; Selloni, A.; Rotzinger, F. P.; Gratzel, M. *Phys. Rev. Lett.* **1998**, *81*, 2954–2957.

(32) Gong, X. Q.; Lu, G.; Selloni, A. *J. Phys. Chem. C* **2008**, *112*, 6594–6596.

(33) Liu, S. W.; Yu, J. G.; Jaroniec, M. *J. Am. Chem. Soc.* **2010**, *132*, 11914–11916.

(34) Ma, X. Y.; Chen, Z. G.; Hartono, S. B.; Jiang, H. B.; Zou, J.; Qiao, S. Z.; Yang, H. G. *Chem. Commun.* **2010**, *46*, 6608–6610.

(35) Zhang, D.; Li, G.; Yang, X.; Yu, J. C. *Chem. Commun.* **2009**, *29*, 4381–4383.

(36) Han, X.; Kuang, Q.; Jin, M.; Xie, Z.; Zheng, L. *J. Am. Chem. Soc.* **2009**, *131*, 3152–3153.

(37) Zhu, J.; Wang, S.; Bian, Z.; Xie, S.; Cai, C.; Wang, J.; Yang, H.; Li, H. *Cryst. Eng. Commun.* **2010**, *12*, 2219–2224.

(38) Yang, X. H.; Li, Z.; Liu, G.; Xing, J.; Sun, C.; Yang, H. G.; Li, C. *Cryst. Eng. Commun.* **2011**, *13*, 1378–1383.

(39) Chen, J. S.; Tan, Y. L.; Li, C. M.; Cheah, Y. L.; Luan, D.; Madhavi, S.; Boey, F. Y. C.; Archer, L. A.; Lou, X. W. *J. Am. Chem. Soc.* **2010**, *132*, 6124–6130.

(40) Fang, W. Q.; Zhou, J. Z.; Liu, J.; Chen, Z. G.; Yang, C.; Sun, C. H.; Qian, G. R.; Zou, J.; Qiao, S. Z.; Yang, H. G. *Chem.—Eur. J.* **2011**, *17*, 1423–1427.

(41) Cho, C. H.; Ho, C. H.; Han, M. H.; Kim, D. H.; Kim, D. K. *Mater. Chem. Phys.* **2005**, *92*, 104–111.

(42) Dinh, C. T.; Nguyen, T. D.; Kleitz, F.; Do, T. O. *ACS Nano* **2009**, *3*, 3737–3743.

(43) Joo, J.; Kwon, S. G.; Yu, T.; Cho, M.; Lee, J.; Yoon, J.; Hyeon, T. *J. Phys. Chem. B* **2005**, *109*, 15297–15302.

(44) Xiang, Q.; Yu, J.; Jaroniec, M. *Chem. Commun.* **2011**, *47*, 4532–4534.

(45) Brunauer, S.; Emmet, P. H.; Teller, E. *J. Am. Chem. Soc.* **1938**, *60*, 309–319.

(46) Barret, E. P.; Joyner, L. G.; Halenda, P. P. *J. Am. Chem. Soc.* **1951**, *73*, 373–380.

(47) Adamski, A.; Spalek, T.; Sojka, Z. *Res. Chem. Intermed.* **2003**, *29*, 793–804.

(48) Fittipaldi, M.; Curri, M. L.; Comparelli, R.; Striccoli, M.; Agostiano, A.; Grassi, N.; Sangregorio, C.; Gatteschi, D. *J. Phys. Chem. C* **2009**, *113*, 6221–6226.

(49) Hurum, D. C.; Gray, K. A.; Rajh, T.; Thurnauer, M. C. *J. Phys. Chem. B* **2005**, *109*, 977–980.

(50) Hurum, D. C.; Agrios, A. G.; Crist, S. E.; Gray, K. A.; Rajh, T.; Thurnauer, M. C. *J. Electron Spectrosc.* **2006**, *107*, 155–163.

(51) Hurum, D. C.; Agrios, A. G.; Gray, K. A.; Rajh, T.; Thurnauer, M. C. *J. Phys. Chem. B* **2003**, *107*, 4545–4549.

(52) Berger, T.; Sterrer, M.; Diwald, O.; Knözinger, E.; Panayotov, D.; Thompson, T. L.; Yates, J. T. *J. Phys. Chem. B* **2005**, *109*, 6061–6068.

(53) Elser, J. E.; Berger, T.; Sterrer, M.; Brandhuber, D.; Bernardi, J.; Diwald, O.; Knozinger, E. *J. Phys. Chem. B* **2006**, *110*, 7605–7608.

(54) Scotti, R.; D'Arienzo, M.; Testino, A.; Morazzoni, F. *Appl. Catal., B* **2009**, *88*, 497–504.

(55) Scotti, R.; Bellobono, I. R.; Canevali, C.; Cannas, C.; Catti, M.; D'Arienzo, M.; Musinu, A.; Polizzi, S.; Sommariva, M.; Testino, A.; Morazzoni, F. *Chem. Mater.* **2008**, *20*, 4051–4061.

(56) Dimitrijevic, N. M.; Saponjic, Z. V.; Rabatic, B. M.; Poluektov, O. G.; Rajh, T. *J. Phys. Chem. C* **2007**, *111*, 14597–14601.

(57) Kevan, L., Schwartz, R. N., Eds. *Time Domain Electron Spin Resonance*; Wiley, Inc.: New York, 1979.

(58) Berger, T.; Diwald, O.; Knozinger, E.; Sterrer, M.; Yates, J. T. *Phys. Chem. Chem. Phys.* **2006**, *8*, 1822–1826.

(59) Carter, E.; Carley, A. F.; Murphy, D. M. *J. Phys. Chem. C* **2007**, *111*, 10630–10638.

(60) Howe, R. F.; Gratzel, M. *J. Phys. Chem.* **1987**, *91*, 3906–3909.